

*Hubble Space Telescope Images of Magellanic Cloud Planetary
Nebulae: Data and Correlations across Morphological Classes*¹

L. Stanghellini^{2,3,4}

J. C. Blades²

S. J. Osmer^{2,5}

M. J. Barlow⁶

X.-W. Liu⁶

¹Based on observations made with the NASA/ESA Hubble Space Telescope, obtained at the Space Telescope Science Institute, which is operated by the Association of universities for research in Astronomy, Inc., under NASA contract NAS 5-26555

²Space Telescope Science Institute, 3700 San Martin Drive, Baltimore MD 21218, USA

³Affiliated to the Astrophysics Division, Space Science Department of ESA

⁴*on leave*, Osservatorio Astronomico di Bologna

⁵Present address: Department of Computer Sciences, University of Edinburgh, King's Buildings, Mayfield Road, Edinburgh EH9 3JZ, Scotland

⁶Department of Physics and Astronomy, University College London, Gower Street, London WC1 6BT, UK

Received _____; accepted _____

ABSTRACT

The morphology of planetary nebulae (PNe) provides an essential tool for understanding their origin and evolution, as it reflects both the dynamics of the gas ejected during the TP–AGB phase, and the central star energetics. Here we study the morphology of 27 Magellanic Cloud planetary nebulae (MCPNe) and present an analysis of their physical characteristics across morphological classes. Similar studies have been successfully carried out for galactic PNe, but were compromised by the uncertainty of individual PN distances. We present our own HST/FOC images of 15 Magellanic Cloud PNe (MCPNe) acquired through a narrow-band $\lambda 5007$ [O III] filter. We use the Richardson–Lucy deconvolution technique on these pre–COSTAR images to achieve post–COSTAR quality. Three PNe imaged before and after COSTAR confirm the high reliability of our deconvolution procedure. We derive morphological classes, dimensions, and surface photometry for all these PNe. We have combined this sample with HST/PC1 images of 15 MCPNe, three of which are in common with the FOC set, acquired by Dopita *et al.* (1996), to obtain the largest MCPN sample ever examined from the morphological viewpoint. By using the whole database, supplemented with published data from the literature, we have analyzed the properties of the MCPNe and compared them to a typical, complete galactic sample. Morphology of the MCPNe is then correlated with PN density, chemistry, and evolution.

Subject headings: Planetary Nebulae: Morphology, Evolution – Magellanic Clouds

1. Introduction

Planetary Nebulae (PNe) provide a fertile ground for studying the evolution of low and intermediate mass ($M \leq 8 M_{\odot}$) stars. The morphology of PNe, when combined with the physical properties of the nebulae and the central stars (CS's), help to complete the picture of how such stars evolve and how the evolution depends on mass, chemical content, and PN environment. PNe are in fact stellar envelopes ejected in advanced evolutionary stages, and carry a wealth of information on previous phases.

The morphology of PNe, as observed through narrow-band filters, traces the structure of the ejected gas, and contains information on the time interval between ejection and observation, in addition to the nature of the ejection itself; the final ionized gas shape contains information on inhomogeneities during ejection. Morphological characteristics change with both the nebular and stellar evolution, thus they carry a record of the space and time history between the ejection and the observation. The ejecta can be perturbed, for instance, by a fast CS wind, stellar companions, planets in the central star's system, interstellar medium condensations, magnetic fields, and by changes in the post-ejection stellar evolutionary paths.

To date, several ground-based surveys of galactic PNe aimed at delineating their morphological characteristics have been completed (Schwarz, Corradi, & Melnick 1992; Manchado *et al.* 1996; Chu, Jacoby, & Arendt 1987; Balick 1987). A space-based survey of galactic PNe has been performed by Bond *et al.* (1995) with the WFPC2 camera on board the HST. Shapes of planetary nebulae have been carefully classified and cross-correlated with nebular and stellar properties, obtaining a series of interesting results, ranging from the segregation of PNe hosting different types of central stars based on their morphology (Calvet & Peimbert 1983; Stanghellini, Corradi, & Schwarz 1993) to the indication that bipolar PNe have more massive progenitors than elliptical PNe (Stanghellini *et al.* 1993;

Corradi & Schwarz 1994). However, such results need also to be tested in a distance–bias free environment.

Only a handful of galactic PNe have individually determined distances, while the majority have distances derived with a statistical method, based on physical assumptions, such as, for example, that all optically thin PNe in the Galaxy share the same ionized mass (Cahn, Kaler, & Stanghellini 1992; Kingsburgh & Barlow 1992). Not only are the absolute stellar and nebular parameter determinations at risk when using poorly determined distances, but even the morphologies themselves could be misclassified when compared to one another and thought to be, for example, at the same distance from us, since the detectability of morphological details obviously decreases with distance. The proximity of the Magellanic Clouds have made them perfect target galaxies to study PNe in a distance–bias free environment. However, use of the cameras aboard HST is required to resolve the shape of the Magellanic Cloud PNe (MCPNe). The spatial resolution of HST/FOC allows observation of MCPN morphology with similar definition to typical galactic PNe at a distance of ≈ 1.5 kpc observed from the ground with 1 arcsec seeing.

Only nineteen narrow–band HST frames of MCPNe have been published to date, either imaged with the PC1 (Dopita *et al.* 1996, hereafter D96) or the Faint Object Camera (Blades *et al.* 1992, hereafter B92). All published data were acquired in the pre–COSTAR, pre–first refurbishing mission epoch (<1994). The B92 paper is an essay on what can be achieved with HST/FOC when observing MCPNe through the $H\beta$ and [O III] narrow–band filters. B92 showed, for the first time, spatially resolved images of four extragalactic PNe and their morphological details. The target nebulae were chosen to be bright, so as to trace early post–AGB evolution. Liu *et al.* (1995) used B92’s images to construct detailed photoionization models for two of these nebulae, SMC N 2 and N 5, derived nebular ionized masses and central star masses, and compared nebular expansion ages

with central star evolutionary track ages. The main aim of the GO observing program of D96 was to image, through the narrow-band [O III] filter, a number of MCPNe covering a large domain in nebular parameter space, such as [O III] luminosity, luminosity class and optical thickness. Their published results included the narrow-band images and the study of the expansion velocities and dynamical ages, taking into account the nebular inclination on the plane of the sky in the case of non-symmetric PNe. The resulting nebular evolution was then coupled with a study of the evolutionary status of the central stars, by means of the $\log T$ – $\log L$ plane location. Dynamical ages and evolutionary times were found not to follow a simple correlation if the evolutionary times were calculated on the basis of hydrogen-burning; rather, the authors suggested in D96 that nebulae hosting helium-burning CS's outnumbered by 2:1 those hosting H-burning CS's.

The main purpose of the present paper is to present previously unpublished narrow-band images of MCPNe, taken with the FOC as part of the original FOC Investigation Definition Team science program. Most of the images presented here were acquired before COSTAR was installed on the HST. However, three MCPNe were re-observed following the first servicing mission, using the FOC and COSTAR to check on the reliability of the original images and the veracity of the deconvolution method used in their analysis. We present the data as follows. In Section 2 we discuss the observations obtained with the FOC, including target-selection criteria, scheduling of the observations, data reduction and calibration, with emphasis on the deconvolution method. Results from the FOC observations are presented in Section 3 for the complete HST/FOC data set, i.e., the newly observed PNe and the ones published by B92; we discuss [O III] images only. Additionally, we have broadened the MCPN database by reclassifying the PC1 images from D96 with the same morphological scheme used for the FOC data. So, in Section 3 we show (a) the final deconvolved FOC frames, (b) the morphological classification, (c) the MCPN dimensions, (d) the photometry, and (e) the expansion velocity and the dynamical ages, and discuss the

results in Section 4. The conclusions, and a discussion of possible future developments, are in Section 5.

2. HST/FOC observations and reductions

17 MCPNe have been observed since June 1991 over 4 HST observing cycles, using the high resolution f/96 optical chain of the Faint Object Camera (Macchetto *et al.* 1991). The observations concentrated on using the narrow-band F501N filter to record the [O III] lines, while a few of the objects were also recorded in the narrow-band H β filter F486N. The H β recombination line traces emission by the dominant element in the nebula, while the [O III] λ 5007 transition is a strong, collisionally excited, cooling line which traces emission by the usually dominant O⁺⁺ ion of oxygen. The systemic radial velocities of the Small and Large Magellanic Clouds shift the [O III] lines by between +2 and +5 Å relative to their rest wavelengths, putting the λ 5007 member of the [O III] doublet at the peak of the filter’s transmission. With a total bandpass of 74 Å, the weaker member of the doublet at 4959 Å will not be transmitted through the F501N filter, according to the transmission curve given in the current FOC Handbook (Nota *et al.* 1994).

This program was originally planned before the launch of HST, and the targets were chosen to be easily detected through the selected filters in reasonable exposure times and without any image saturation. The nebulae were thus chosen to be reasonably bright in the λ 5007 [O III] line. In order to maximize the probability that the chosen nebulae were optically thin, and thus that the ionized masses would be equal to the true nebular masses, two additional selection criteria were used: (a) the nebulae should have a detectable λ 4686 He II line, a standard criterion for selecting out low- and medium-excitation PNe with younger and less evolved central stars (Sanduleak, MacConnell, & Philip 1978); and (b) the nebulae should have [O II] electron densities less than about 5000 to 6000 cm⁻³. The optical

spectroscopic study of Barlow (1987) had indicated this to be the dividing point between optically thick and optically thin Magellanic Cloud PNe. The analysis by Liu *et al.* (1995) subsequently confirmed that SMC N 2 with $n_e(\text{O II}) = 2850 \text{ cm}^{-3}$ and $3727/\text{H}\beta = 0.29$ is indeed optically thin but they found that SMC N 5 with $n_e(\text{O II}) = 3890 \text{ cm}^{-3}$ and $3727/\text{H}\beta = 0.79$ is still optically thick.

Most of the observations were obtained in the observing cycles before the 1993 December servicing mission which repaired the imaging capability, although three LMC objects, N 66, N 97, and N 192, have since been re-observed. As we shall explain, they provide an important check on the analysis of the earlier data. Because of its intriguing morphology, LMC N 66 (SMP 83) was observed on two separate occasions before the servicing mission as well as once afterwards. Our monitoring of this object turned out to be fortuitous because of the recently announced variability in brightness of the central star (Pena *et al.* 1994). Although we use the image of N 66 to check pre-COSTAR deconvolution performance, we do not include this object in the discussion nor in Tables 2 and 3; Vassiliadis (1996) has discussed and interpreted the ensemble of HST FOC and WFPC images of N 66 obtained between 1991 July and 1994 February. Table 1 gives a complete record of the FOC observations in the $[\text{O III}] \lambda 5007$ light. All observations were taken in the 512×512 pixel format with $25\text{-}\mu\text{m}$ square pixels, corresponding on the sky to a plate scale of 0.0223 arcsec per pixel before the servicing mission and 0.0144 arcsec per pixel with the Corrective Optics Space Telescope Axial Replacement (COSTAR) in place (Jedrzejewski *et al.* 1994).

The observations taken after the 1993 December servicing mission were obtained very early in the observing cycle (January and February 1994) and before the correct instrument sensitivities had been determined. Inappropriately, pre-servicing values were in use at that time, resulting in an incorrect value for the keyword PHOTLAM being attached to the

data in the calibration pipeline. Unfortunately, all FOC data taken around that time have been archived with the incorrect value. (This problem was corrected in the FOC calibration pipeline on 19 April 1994.) We have rectified our Cycle 4 data with the proper values. In order to guard against the risk of saturation to the post servicing mission data we obtained a pair of F501N images for N 97 and N 192 by taking a second image with a 1 magnitude neutral density filter, see Table 1.

There are two calibrations that are applied to the raw FOC data in the ground–system calibration pipeline, namely a geometric distortion correction followed by a relative calibration or flat field correction. For the data taken in the early cycles we reprocessed the observations using the IRAF/STSDAS task called CALFOC using new calibration files as they became available, and we have reprocessed all the data originally presented in B92. Finally, we removed by interpolation the effects of the numerous reseaux marks, which are fiducial reference marks engraved on the detector faceplate.

Our earlier analysis (B92) had shown that deconvolution techniques could be employed to improve the qualitative appearance of these compact and high contrast objects. This result encouraged us to continue taking observations throughout the early cycles rather than waiting for the 1993 servicing mission. Accordingly, we spent considerable effort in the reduction phase to try and optimize the deconvolution and to investigate how different point spread functions (PSFs) and the telescope focus were likely to be affecting the accuracy of our data. Subsequently, the three post–COSTAR images were of great value in providing a direct comparison between the data sets and in vindicating our approach.

For deconvolution we used the non–linear restoration technique of Richardson (1972) and Lucy (1974) which has been installed in the IRAF/STSDAS software package, and we performed testing on the optimum number of iterations for our images. In qualitative terms, we found that after 50 iterations the images showed considerable improvement,

through reduction of the surrounding halo or skirt of scattered light while still retaining the basic structure that could be seen in the unprocessed images. After a larger number of iterations (100) the shape and form of the objects began to break down and the images became artificially lumpy and pixilated. We chose 50 iterations for all the pre-COSTAR observations. The same number of iterations was found by Dopita and collaborators to be the best for deconvolving WF/PC images too (Dopita 1998, private communication).

The images obtained in 1994 with COSTAR of LMC N 97 and N 192 were valuable in establishing the veracity of the deconvolution work. In Figure 1 we show contour plots of the deconvolved pre-COSTAR images of these two PNe with the more recent images obtained with FOC and the COSTAR. There is excellent agreement between the pre-COSTAR deconvolved images and the post-COSTAR direct images. The agreement covers the overall size and shapes of the nebulae and extends to the smallest structures that can be discerned at a scale of 0.07 to 0.1 arcsec. The consistency can also be seen in the images that are presented later (see Figure 5, panels 1 and j, and m and n), as well as in the good photometric agreement (see § 3). The direct comparison provides confidence that the deconvolution technique has improved the qualitative appearance of these objects without introducing artifacts.

Routine monitoring of the image quality of HST has been carried out since launch in order to monitor and maintain good telescope focus as well as to characterize the features of the optical performance (Hasan & Burrows 1994). During this time, the Optical Telescope Assembly (OTA) continued a steady contraction as gas desorbed out of the telescope structures, thus requiring frequent re-alignments to retain the focus within 10 microns of the nominal value, and this was not always achieved. In addition, short time period fluctuations of the OTA PSF were discovered (Hasan & Bely 1993) which are attributed to expansion and contraction of the secondary mirror support system causing small (≈ 5

microns) motions of the secondary mirror (breathing). Also, the internal focus of the FOC was optimized on occasions. It is impossible to unravel the effects of these optical changes from our observations because simultaneous PSF observations were not obtained. (Indeed, it would have been time consuming to have attempted to calibrate these defocusing effects, especially the breathing which can alter the PSF by small amounts over short time periods of about 30 minutes.)

We were concerned that these image degradation problems could affect the resolution of our data and we ran tests to see how sensitive our deconvolution results were to different input PSFs. We experimented with a variety of Richardson–Lucy deconvolutions. Observed PSFs were obtained from FOC calibration observations of BPM 16274 through the F501N filter and these observations provided two PSFs, one based on observations from early in Cycle 1 and one from Cycle 3. A search of the FOC archive yielded a third PSF star from April 1992 observations of the SN 1987A field. Finally, we constructed a theoretical PSF using the optical modeling work of Krist (1993). An obvious advantage of the theoretical PSF compared with any of the observed PSFs is the infinite signal–to–noise ratio. Figure 2 shows the four PSFs described above and Figure 3 shows the results from deconvolving the pre–COSTAR image of N 192 with each of these PSFs.

As inspection of Figure 3 confirms that, at the level to which we are working, the Richardson–Lucy deconvolution is not very sensitive to the input PSF. Both the overall shape and most of the small scale structures remain the same over all four images. On closer examination there are subtle changes from one deconvolution to another, and these changes provide an empirical assessment of the overall accuracy of the deconvolution work. In general, high signal–to–noise ratio PSFs gave the best results (higher counts in the peak of the PN image). This seemed a more important parameter than the closeness in time of the PSF to the actual observation. In other words, for our data, a PSF produced from an

observation in 1991 worked at least as well as a PSF produced in a 1993. Probably the breathing phenomenon is destroying any advantage the contemporary PSF may otherwise have had.

The theoretical PSF can be adjusted to fit precisely any observation by matching the Airy ring pattern using a stellar image in the field of the PN. Potentially, this could allow correction for the breathing phenomena. Unfortunately, among our images only that of N 66 has a star (in fact the central star) suitable for such matching. Figure 4 shows the results of matching and not matching the theoretical PSF to the central star. Qualitatively it is difficult to discern the difference between the two; however, the peak counts in the image deconvolved with the matched Airy rings are 20 percent higher, indicating that an improvement is achieved with this method. On the other hand, we found that use of the theoretical PSF tends to yield a rather uneven and blotchy appearance to the image which the observed PSFs do not. In any case, the lack of available stars in the other PN images prevents us from using this approach for cases other than N 66. After considerable testing we selected the 1991 observed PSF to use for all our pre-COSTAR deconvolution work.

A particular concern that we had was whether faint extended halos that might exist around the main nebular structures would be recovered by the deconvolution process, since such halos could potentially contain a significant fraction of the total nebular mass. For example, a faint halo three times larger than that of the main inner structure, and with a mean surface brightness of only 1.5% that at the central peak, would still contain as much mass as in the inner bright nebula. We therefore experimented by artificially adding smooth halos of varying surface brightnesses and diameters to the deconvolved FOC [O III] nebular images of SMC N2, SMC N5 and LMC N192. These composite images were then convolved with an observed PSF and the resulting convolved images were deconvolved with the Richardson-Lucy algorithm in the standard way. It was found that the artificial faint halos

were recovered in the deconvolved images in all cases, down to halo surface brightness levels of 1% of the peak inner emission. We are therefore confident that any halo emission around the brighter PNe in the sample must be below this level, although for the fainter PNe in the sample the upper limits to any surrounding halos would be correspondingly larger. Our re-observations of four of the nebulae, after the installation of the COSTAR corrective optics, revealed no extended low surface brightness emission around them, confirming this conclusion in their cases.

3. Image analysis

3.1. The FOC and PC1 data sets

Our discussion of PN morphologies, dynamical expansion times, and luminosities is based on two data sets. The first data set is composed of the FOC images presented here for the first time and the images illustrated by B92 (FOC set); the other set consists of the PC1 images described by D96 (PC1 set). In all we have 27 MCPNe, excluding N 66 (see § 2). The list of observed PNe can be found, respectively, in Table 1 of this paper for the FOC set, and in D96’s Table 1 for the PC1 set. The two sets have three objects in common, useful to check the criteria for morphological classification, and image quality. Each set has been selected with a defined criterion: the FOC set contains PNe with high [O III] fluxes and generally low optical thickness, while PC1 set presents a variety of [O III] fluxes and Lyman continuum optical depths. As a consequence, the two sets are not homogeneous, and the final composite sample is not, by any means, a complete or unbiased statistical sample of MCPNe. Nonetheless, there is purpose to analysing the composite group of PNe in a qualitative way, in order to establish morphological trends.

3.2. Morphology and diameters

The $\lambda 5007$ [O III] narrow-band FOC images are presented in Figure 5. The pre-COSTAR images are deconvolved, as discussed in Section 2. In Figure 5 we also include three nebulae already published by B92, and we show both the pre-COSTAR (deconvolved) and post-COSTAR images for N 97 and N 192. The following discussion, on the morphology, the dimensions, and the photometry of the PNe observed with the FOC, is based on the [O III] images. To classify the morphology we follow the most recent and widely used scheme by Schwarz, Corradi, and Stanghellini (1992) in its updated version (Manchado *et al.* 1996). Originally, this classification scheme was conceived for $H\alpha$ (or $H\beta$) images, expecting this emission line to track the bulk of ionized gas in most PNe. In the case of the FOC set, whose PNe have high excitation, the morphological differences between high- and medium-excitation plasma tracers are not expected to be significant (for galactic equivalents, browse through high-excitation PN images in the catalog by Machado *et al.* 1996). In the case of the PC1 set, however, the lower excitation might not be fully delineated by the [O III] line. Another source of inhomogeneity among the two data sets is the different angular resolution of the two cameras used in the observations. The PC1 frames published by D96 clearly show their lower angular resolution with respect to the FOC images published here for the first time, or by B92.

The classification scheme sorts PNe into five main groups, as defined by the outer envelope of the PNe: Round PNe (R), Elliptical PNe (E), Bipolar PNe (B), Quadrupolar PNe (Q), and Pointsymmetric PNe (P). Bipolar PNe are nebulae with one axis of symmetry, and a detectable *waist*. Quadrupolar PNe consist of two pairs of bipolar lobes, joined at a common waist. Pointsymmetric PNe show structures that are symmetric with respect to a central point (in 2D). The scheme by Machado *et al.* (1996) does not include “irregular PNe”, although it includes the possibility that a PN could not be classified within the

above scheme, and in this case they are denoted as NC. The main classes have subclasses, denoted by suffixes attached to the morphological main symbols. The subclasses describe inner structures (s), multiple shells or haloes (m), ansae attached to the main structures (a), and rings at the waist of some bipolar nebulae (r).

We can apply the morphological classification scheme to Magellanic Cloud PNe, although we should keep in mind that the [O III] images of these nebulae will track the bright cores rather than outer features, such as multiple shells and bipolar/quadrupolar lobes. In this sense, real bipolar structures may not be observed in their complete display of lobes, rather only the inner ring may be visible. As discussed in Section 2, our analysis of the nebulae confirmed the absence of lobes. We find instead a considerable subgroup of objects whose outer shape is elliptical, and whose inner shape is “bipolar”, showing two concentrations of surface brightness. Such structure is reminiscent of a projected inner ring, that, in turn, is typical of bipolar outflows. From the asymmetry of the ring like structures we can be quite confident that their true morphology is bipolar rather than elliptical. We classify these PNe as *bipolars* (B), subclass *bipolar core* (bc).

Table 2 gives the morphological classification of PNe. In columns (1) and (2) we give the discovery name and SMP (Sanduleak *et al.* 1978) catalog number. Column (3) gives the HST camera used for the observation, where *FOC* indicates the PN whose images are published in this paper for the first time, or by B92, and *PC1* indicates the D96 images. Column (4) defines the morphological class, and the detailed classification in parenthesis. In two particular cases, the shape is incomplete, and we define that particular shape as the suffix ‘inc’. In column (5) and (6) of Table 2 we give the angular and physical diameters of the PNe, respectively in arcsec and parsecs.

Our diameter measurements are a result of a detailed photometric routine, as we describe following. First, we define a geometrical center of the PN on the image, by hand.

Second, we chose for each object a set of (circular) apertures that segment the nebula into annuli. The outermost of these apertures is set at a large distance from the apparent nebular limb. Then we measure the flux in each aperture with the IRAF/PHOT routine, obtaining the sky-subtracted total flux within each aperture. Going outward from the center, we find the maximum total nebular flux. We then plot the relative encircled flux (flux within each aperture divided by the total flux) versus aperture for each nebula, and we read out the aperture encircling 85 % of the total flux. We define the latter aperture to be the physical nebular radius. This procedure has been repeated for pre- and post-COSTAR images for N 97 and N 192, obtaining satisfactory agreement.

Among the 15 diameters measured with the photometric method by us, six objects show the presence of a ring in the relative encircled flux profile: N 4 (Bbc), L 305 (Es), L 536 (E), L 343 (Bbc), N 18 (Bbc), and N 67 (Bbc). This photometric check is a good method to determine which PNe actually show ring-like features. By using the above described method, we had difficulties in finding the outer contour of the nebula N 24, or the size at which its encircled flux become constant. This planetary has a halo/core structure, with FWHB of the bright core measuring 0.23 arcsec. We thus do not give its outer dimensions in Table 2, and we eliminate this object in the discussion of the results and in Figures 6 through 10. Future observations of this particular object are in order.

Our definition of physical radius is, in principle, the same as D96's, and has been chosen this way for uniformity among the two data sets. Nonetheless, of the three objects in common among the two sets, only for one (WS 12) do the two measurements agree. In the cases of N 4 and L 536, both with ring-like profiles, the measurements are different. The difference can be ascribed to the power-law skirts produced by incomplete deconvolution of the PC1 set, and adds an extra uncertainty to our discussion. For the PC1 set we derived the angular sizes from the published physical sizes (see Table 3 in D96) and the distances

to the Clouds quoted therein ($d_{\text{LMC}}=50.60$ and $d_{\text{SMC}}=58.29$ kpc). Obviously the same distances to the Clouds have been used to derive physical sizes for the FOC set.

Below, we explore in some detail the individual morphologies of those nebulae whose structures are not spherically symmetric. For PNe showing an asymmetric structure, we estimate the projection angle on the plane of the sky, measured from the ratio of the semiminor to the semimajor axes of the ring-like structures, and we have included this axial ratios, q , in Table 3.

N 2 is a regular ellipse with an inner hole.

N 4 has an elliptical, *boxy* shape with evidence of an inner, projected ring. D96 classified it as *BR* (bipolar/ring), which, apart from the different terminology, corresponds to our definition.

N 5 is almost round, with an inner hole.

N 18 has a fairly round outer shell, and an inner, edge-on ring.

L 305 is elliptical; contour levels show a marked asymmetric structure in the inner parts, as if the maximum brightness was off-center.

N 67 resembles a ring feature of a galactic bipolar PN (e. g. NGC 650, Sh 1–89, Manchado *et al.* 1996); the measured inclination of the ring is approximately 45 degrees on the plane of the sky.

L 343 is elliptical with a ring-like core.

L 536 is elliptical, with low ellipticity. D96 defined it as *s* (spherical), while we can actually measure an axial ratio of about 0.8.

LM2–5 is elliptical, with an asymmetric ring-like core.

N 97 shows four density enhancements, and can be classified as quadrupolar.

N 24 has a very slightly elliptical outer shell, and a regular round inner shell, and can be classified as R.

N 192 has a slightly elliptical outer shell, an irregular inner structure, and presents an inner hole. It is classified as R.

WS 12 has elliptical contours, with an incomplete crescent–shape structure. Although D96 classified it as *BR*, we could not definitely see the complete ring with our FOC image brightness analysis.

WS 16 is a ring–like structure, of elliptical contour; we classify it as Es.

LM1–27 has an irregular inner structure, reminiscent of an incomplete ring.

N 122: although D96 found a bipolarity on the deconvolved image, we could not find it on their raw image, which, on the contrary, shows a genuine elliptical PN, with very high ellipticity.

N 52 is elliptical with an inner hole.

LMC SMP 72 is very hard to classify. At a first glance it could resemble a quadrupolar, but a careful analysis shows no evidence for the second pair of rings. It can be a bipolar with an enhanced, large ring.

N 60: our morphological classification confirms that of D96, of spherical/round shape.

N 215 is elliptical with a bipolar core.

LMC SMP 96 is elliptical with a bipolar core.

LM1–61 is round, with irregular inner brightness.

3.3. Aperture photometry of FOC images

Aperture photometry has been performed for the FOC images. Calibrated, but non-deconvolved, images were used to this end. Even if most PNe are easily contained in a 2×2 arcsec² aperture, we chose an aperture of 6 arcsec², since pre-COSTAR images may contain considerable energy output out to 4 arcsec from the target centers. We measured the total counts per second within the aperture, after sky subtraction (Tab. 1, col. [8]), the peak counts per second (Tab. 1, col. [9]) and the calibrated physical fluxes (Tab. 1, col. [10], in erg cm⁻² s⁻¹). The derived FOC [O III] $\lambda 5007$ line fluxes show excellent agreement with the ground-based values measured by Jacoby, Walker, & Ciardullo (1990). For 21 FOC measurements, the mean flux difference is found to be just 0.00 ± 0.02 dex.

3.4. Expansion velocities and dynamical expansion ages

In order to evaluate the dynamical expansion ages of our PNe we need their expansion velocities. We have used velocities based on measurements published by Dopita *et al.* (1985 for SMC, 1988 for LMC PNe). We should beware that Dopita *et al.* define the expansion velocity as 0.911 times the FWHM of the $\lambda 5007$ [O III] line, corrected for instrumental and thermal broadening, whereas in general (e.g. in the galactic PN expansion velocity catalogs of Sabbadin 1984 and Weinberger 1989) the value $v_{\text{exp}} = 0.50$ FWHM is used for unresolved nebulae⁷. We use this second choice for the expansion velocity, and corrected the velocities of Dopita *et al.* as if they have been measured in this way, thus dividing them by 1.82. The

⁷Robinson, Reay & Atherton (1982) have shown theoretically that the FWHM linewidth of a nebula completely enclosed by an observing aperture is equal to the line splitting that would be observed at the nebular center in a spatially resolved observation. Munch, Hipplein, & Pitz (1984) have confirmed this result observationally

resulting nebular expansion velocities are given in Table 3, column (3) ⁸.

Column 4 of Table 3 lists $\tau_{\text{dyn}} = R_{\text{neb}}/v_{\text{exp}}$, the dynamical expansion ages derived from the PN radii and expansion velocities (where R_{neb} is half the diameter D listed in col. 6 of Table 2). Table 3 (col. 2) also lists q , the measured ratio of the nebular semi-major to semi-minor axes. D96 made use of this parameter to correct dynamical expansion times for nebular inclination effects, assuming that ring-shaped nebulae are circles viewed at an inclination angle $\theta = \cos^{-1}q$ with respect to the plane of the sky, so that measured expansion velocities should be corrected for inclination effects by dividing them by $\sin \theta$. However, since this would yield infinite expansion velocities and zero expansion ages for $q = 1$, no correction was made for circular nebulae. We found that the use of this scheme led to large decreases in the derived expansion ages for nearly-circular nebulae (e.g. a factor of 2.5 for SMC N2, with $q = 0.92$), versus no correction at all for perfectly circular nebulae (e.g. SMC N5, $q = 1.0$) and so decided not to make such a correction. We note that for non-circular nebulae the nebular radius defined by the 85% encircled energy definition is in any case a mean of the semi-major and semi-minor axis dimensions, so that its use yields dynamical ages that are smaller than those that would be obtained just from

⁸ The FWHM of a Gaussian line profile contains 76% of its total flux. Dopita *et al.* (1985) defined the expansion velocity as the half-width at one tenth maximum line intensity. For a Gaussian, the full width corresponding to this definition contains 97% of the total line flux. For comparison, the nebular diameter definition adopted by D96 and by ourselves is the diameter encircling 85% of the total nebular flux. For a Gaussian line profile, 85% of the total line flux is contained within 0.4 maximum line intensity. We prefer to adopt here the usual definition of $v_{\text{exp}} = 0.5$ FWHM, but if expansion velocities corresponding to the half width at 0.4 maximum line intensity are preferred, then the derived expansion ages in Table 3 should be decreased by a factor of 1.15.

the semi-major axis dimensions. We note that barrel-shaped nebulae can yield apparent circular shapes when viewed pole-on, and elliptical shapes when viewed equator-on. Figs. 4 and 5 of Frank & Mellema (1994) show that for such nebulae viewed pole-on the measured expansion velocity corresponds to material along the line of sight that is expanding in the polar (longer axis) direction, with a velocity higher than that in the equatorial direction. Thus dynamical ages for apparently near-circular nebulae of this type may therefore be underestimated, since they could be using too high an expansion velocity.

4. Analysis of the results

The morphologies of the 27 MCPNe in the [O III] narrow band images are similar to those of galactic PNe, if we consider the bright parts of the latter ones. We did not find multiple shell PNe or faint extended lobes of bipolar and quadrupolar PNe. Similarly to galactic PNe, we encounter round, elliptical, bipolar (ring), and quadrupolar shapes. We did not expect that the statistical distribution among our group of MCPNe would be the same as for galactic PNe, since we have overall selected against faint and low excitation PNe, thus against symmetric shapes (Stanghellini *et al.* 1993). We found that 36% of the studied MCPNe are round, 32% are elliptical, and 32% have bipolar or quadrupolar shapes. The northern galactic sample (Manchado *et al.* 1996) has 24% round, 56% elliptical, 17% bipolar and quadrupolar, and 3% pointsymmetric PNe. We thus confirm the existence of three main morphological classes, round, elliptical, and bipolar/quadrupolar PNe. We did not find pointsymmetric PNe, nor did we expect them, given the low percentage of occurrence of this particular morphology among galactic PNe. We confirm that more bipolar PNe can be found among high excitation objects, as was already inferred from Zanstra analysis by Stanghellini *et al.* (1993). Our statistical analysis cannot proceed any further, given that we do not have a statistically significant sample.

The main advantage of studying MCPNe with respect to their galactic counterparts resides in knowing their distances. Distance–dependent physical properties, such as physical dimensions, dynamical times, and luminosities, are readily determined for MCPNe. When we discuss dynamical times derived from physical dimensions, we should not overlook the fact that some nebulae are optically thick to the ionizing radiation from the central stars. If a PN should remain optically thick for most of its evolution, its measured diameter would not trace the dynamical evolution, but rather the evolution of the ionization front. We have sorted our PNe according to their optical thickness, as derived from the line ratio $\lambda 3727$ [O II] / $H\beta$. As Kaler & Jacoby (1990) pointed out, this ratio should be higher than 0.8 and 0.35 for, respectively, LMC and SMC PNe to be optically thick. We derive the diagnostic ratio from spectral line intensities available in the literature (Meatheringham & Dopita 1991ab; Vassiliadis *et al.* 1992), and report the optical thickness in Table 2, Column (7). This measure of thickness is rather crude, in that it does not take into account variations of the diagnostic ratio with density, thus a small fraction of PNe labeled as *thin* in Table 2 might be in fact thick. The results of Table 2 agree for the most part with Dopita and Meatheringham’s (1991ab) photoionization models optical thickness, which we do not use therein to avoid model dependence.

Among those PNe whose diagnostic spectral lines are available in the literature, we find that (a) about half the elliptical PNe are optically thin, (b) most round PNe are optically thin according to the above criterion, and (c) only one asymmetric (bipolar) PN is optically thin. Obviously the fact that the majority of PNe in the FOC set are optically thin to the ionizing radiation strongly depends on the target selection of those planetaries, but the thickness/thinness of each morphological class was not selected a priori. Since most bipolar/quadrupolar PNe are thick to ionizing radiation, their measured physical size can be an underestimate of the real size, and the dynamical time could be actually larger than calculated.

In Figure 6 we plot the histogram distributions of three main nebular properties: physical dimensions (top), expansion velocities (middle), and dynamical expansion ages (bottom). Each morphological class is represented in a different way (see caption). we infer the following properties: (a) bipolar PNe have dimensions larger than 0.2 pc, this result, although based on very few objects, is an important confirmation of a similar situation existing for galactic PNe (Stanghellini 1995); (b) bipolar PNe in our sample have physical dimensions within a narrower range than elliptical and round PNe.

In Figure 7 we examine the time evolution of the PN sizes for three major morphological classes: round, elliptical, and asymmetric (bipolar and quadrupolar) PNe. We did not include those PNe whose angular size is a measured upper limit (see D96). The physical dimensions correlate linearly with the dynamical ages, as expected, with scatter due to the velocity distribution. In particular, elliptical and bipolar/quadrupolar PNe define a very tight correlation, with coefficient $R_{xy}=0.92$.

We can use the physical dimensions and dynamical age as independent variables to reveal correlations with other physical parameters across morphological classes. Due to the limited size of our sample and the selection criteria of the targets, the range of physical diameters is rather restricted, and each morphological class is not statistically represented. When using the dynamical age as an indication of the evolutionary timescale, we should not overlook the fact that it merely indicates the time lapse between the envelope ejection at the TP–AGB phase and the observing time, and assumes a constant expansion velocity without acceleration (or deceleration) or the shell. τ_{dyn} is a very useful variable for order of magnitude correlations, but it does not indicate the exact lifetime of a PN. Furthermore, since zero age post–AGB tracks generally correspond to a defined central star temperature, one can really never finely tune these tracks to the observed dynamical times, and a direct comparison among the two sets of parameters, the theoretical ones and the empirical,

should not be used without precautions (Käufel, Renzini, & Stanghellini 1993). On the other hand, dynamical ages measured for MCPNe are generally more homogeneous than those measured for galactic PNe since their distances are better known and the dimensions and the velocities of the MCPNe both correspond to the high excitation body of the PN.

Electron densities, measured from forbidden line ratios, have been plotted in Figure 8 against the physical dimensions of the MCPNe. The general trend shows a decreasing electron density with increasing physical size, with the exception of L 305 and N 67, whose loci are in the upper-right part of the diagram.

In order to study the fading of PNe with evolution, accordingly to their shapes, we have analyzed the [O III] surface brightness. The [O III] luminosities from which we derive the surface brightness have been calculated from the total fluxes observed from the ground (Jacoby *et al.* 1990), the Cloud distances, and the extinction constant (Boffi & Stanghellini 1994, and references therein). The correction for extinction has been performed using the galactic extinction curve (Osterbrock 1989), which around 5007 \AA has a similar shape to the curve derived for the Magellanic Clouds (Hoyle & Wickramasinghe 1991). Figure 9 aims at disclosing possible evolutionary effects on the surface brightness for PNe of different shapes. The [O III] luminosity depends on the stellar energetics, and secondarily on the oxygen content and on the effects of nebular evolution (Richer 1993). It is thus a good guide for tracing the intrinsic stellar luminosity.

What we see in plot 9 is that the round PNe (symbols are as in the other Figures) are not to be found at low surface brightness, as opposed to elliptical/bipolar/quadrupolar PNe. One reason for the split in fading behaviors could certainly be a difference in the ionized masses, which, in turn, could be an indication for a difference in the mass of the progenitors (see Fig. 8 in Boffi & Stanghellini, 1994). On the other hand, a systematic difference of velocity fields among the round PNe and all other shapes can also produce

such a separation as in Figure 9. Indeed, the relation between the axial ratio q and v_{exp} shows that extreme asymmetric PNe do evolve faster. But the velocity difference alone does not explain the discrimination among morphological types of Figure 9. Unfortunately, given the small size of the sample, and that most of the PNe in the Figure are optically thick to ionizing radiation, we can not conclude that we are observing two groups of PNe with different progenitor masses. What we are probably seeing here is that more massive stars evolve faster through the high luminosity post-AGB phase, and they are fading at the time of observation. On the other hand, stars with low-mass progenitors evolve slowly, thus retaining their high luminosity for a longer time. Should this interpretation be right, we can conclude that most bipolar/quadrupolar and elliptical PNe in our sample have high mass progenitors, while most round PNe have low-mass progenitors, in addition to lower velocities. Only with a much larger and homogeneous sample of MCPNe we could investigate this important aspect of PN evolution to its fullness. Accurate modeling of the surface brightness evolution of expanding shell and ring PNe are also required to provide the necessary background to complete the picture.

In order to confirm the nature of the asymmetric PNe in our sample, and to test the correlation between morphology and chemical enrichment, as found by Peimbert and collaborators (e.g., Calvet & Peimbert 1983, Peimbert & Torres-Peimbert 1983), in Figure 10 we plot the N/O abundance ratio against dynamical expansion time for all PNe for which the N/O ratio is available (Richer 1993). Symbols are for the different nebular shapes, as in the other Figures. Since the (revised) N/O abundance ratio constraints for Type I PNe are different for SMC, LMC and Galactic PNe (Kingsburgh & Barlow 1994, Peimbert 1997), we have artificially decreased the N/O abundance ratio of SMC PNe by an appropriate factor, so that they can be directly compared ($\Delta \log \text{N/O}=0.24$). The horizontal line in Fig. 10 is at the appropriate level so that PNe above the line are of Type I (see note *a* on Table 2 for PNe identification). We find that all round PNe in our sample are non-Type I, all but

one bipolars are Type I, and elliptical PNe are equally divided among the two Peimbert Types. We do not see any evolution in the N/O abundance. The number of objects is so low to leave the possible consequences unexplored for now. What we can infer from the last two Figures is that round and bipolar/quadrupolar PNe form two distinct “enrichment” groups, while more investigation is necessary to determine whether the ellipticals are an intermediate sequence or a different evolutionary stage of either round or bipolar nebulae.

5. Conclusions

We have presented a set of narrow-band images of 15 Magellanic Cloud Planetary Nebulae acquired with the FOC, aboard the Hubble Space Telescope. Deconvolution techniques, and comparison to post-COSTAR FOC images of three of the PNe, show that excellent image quality can be achieved from pre-COSTAR images. We have measured the nebular angular diameters, allowing the calculation of dynamical expansion ages, when combined with the known distances to the Magellanic Clouds and previously measured expansion velocities. We have used the published PC1 MCPN images from D96, and other relevant physical parameters from the literature, to obtain a total group of *27 extragalactic planetary nebulae with known distance, morphology, and dynamical age*, by classifying all the PNe with the same morphological scheme. The main scientific content of this paper is the presentation, discussion, and analysis of the new MCPN data acquired with HST/FOC. We also attempted a limited analysis of nebular properties across morphological classes. The results suffer from low statistics, especially within each class. Nonetheless, we find some trends that would confirm previous studies on galactic PNe, mainly, that symmetric and asymmetric PNe seem to belong to different brightness group (in the $\lambda 5007$ [O III] line), possibly indicating that they belong to different mass groups. In order to have greater consistency in these results, we would need to discuss at least 20 objects for

each morphological class, that is, a sample of a hundred MCPNe observed with the HST cameras. Moreover, although the morphological classification is feasible using pre-COSTAR images, the photometric measurements can suffer considerable errors; it is thus necessary to repeat and extend the analysis to post-COSTAR images of MCPNe. More insight into the evolutionary paths of different nebular shape classes could be achieved by investigating the morphological properties of the MCPNe together with their central stars. The analysis of the sample of MCPNe presented in this paper, together with their central stars, is in progress and will be published in the future.

Thanks to D. Shaw for discussions on the correlation between nebular morphology and stellar evolution in the Clouds, and to M. Dickinson for helping with the IRAF routines. The referee of this paper, M. Dopita, is thanked for his insight and very useful comments. L.S. gratefully acknowledge the hospitality at the Space Telescope Science Institute, where this work was completed. J. C. B. acknowledge support from NASA through the contract NAG5-1733.

REFERENCES

- Balick, B. 1987, AJ, 94, 671
- Barlow, M. J. 1987, MNRAS, 227, 161
- Blades J. C., *et al.* 1992, ApJ, 398, L44 (B92)
- Boffi, F. R., & Stanghellini, L. 1994, A&A, 284, 248
- Bond, H. E., Schaefer, K. G., Fullton, L. K., & Ciardullo, R. 1995, BAAS, 187, 8005
- Cahn, J. H., Kaler, J. B., & Stanghellini, L. 1992, A&AS, 94, 399
- Calvet N., & Peimbert M. 1983, Rev. Mex. Astron. Astrof., 5, 319
- Chu, Y–H., Jacoby, G. H., & Arendt, R. 1987, ApJS, 64, 529
- Corradi, R. L. M., & Schwarz, H. E. 1994, A&A, 293, 871
- Dopita, M. A., Lawrence, C. J., Ford, H. C., & Webster, B. L. 1985, ApJ, 296, 390
- Dopita, M. A., Meatheringham, S. J., Webster, B. L., Ford, H. C. 1988, ApJ, 327, 639
- Dopita, M. A., & Meatheringham, S. J. 1991a, ApJ, 377, 480
- Dopita, M. A., & Meatheringham, S. J. 1991b, ApJ, 367, 115
- Dopita, M. A., *et al.* 1996, ApJ, 460, 320 (D96)
- Frank, A., & Mellema, G. 1994, ApJ, 430, 800
- Hasan, H., & Burrows, C. J. 1994, Proc. SPIE, Vol 1945, p. 36
- Hasan, H., & Bely, P. Y. 1993, BAAS, 183, 113.06
- Hoyle, F., & Wickramasinghe, N. C. 1991, “The Theory of Cosmic Grains”, (Dordrecht: Kluwer)
- Jacoby, G. H., Walker, A. R., & Ciardullo, R. 1990, ApJ, 365, 471

- Jedrzejewski, R. I., Hartig, G., Jakobsen, P., Crocker, J. H., & Ford, H. C. 1994, *ApJ*, 435, L7
- Kaler, J. B., & Jacoby, G. H. 1990, *ApJ* 362, 491
- Käuff, H. U., Renzini, A., & Stanghellini, L. 1993, *ApJ* 410, 251
- Kingsburgh, R. L., & Barlow, M. J. 1992, *MNRAS*, 257, 317
- Kingsburgh, R. L., & Barlow, M. J. 1994, *MNRAS*, 271, 257
- Krist, J. 1993, *ADASS II*, A. S. P. Conf. Ser., Vol. 52, R. J. Hanisch, R. J. V. Brissenden, & J. Barnes (eds.), p. 536
- Liu, X.-W., Barlow, M. J., Blades, J. C., Osmer, S., & Clegg, R. E. S. 1995, *MNRAS*, 276, 167
- Lucy, L. B. 1974, *AJ*, 79, 745
- Macchetto, F., *et al.* 1991, *ApJ*, 369, L55
- Manchado, A., Guerrero, M., Stanghellini, L., & Serra-Ricart, M. 1996, “The IAC Morphological Catalog of Northern Galactic Planetary Nebulae” (Tenerife: IAC)
- Meatheringham, S. J., & Dopita, M. A. 1991a, *ApJS*, 75, 407
- Meatheringham, S. J., & Dopita, M. A. 1991b, *ApJS*, 76, 1085
- Munch, G., Hipplelein, H., & Pitz, E. 1984, *A&A*, 135, L11
- Nota, A., Jedrzejewski, R., Greenfield, D. P., & Hack, W. 1994, “Hubble Space Telescope Faint Object Camera Instrument Handbook” (post-COSTAR), version 5.0
- Osterbrock, D. E. 1989, “Astrophysics of Gaseous Nebulae and Active Galactic Nuclei”, (Mill Valley: University Science Books)
- Peimbert M., & Torres-Peimbert, S. 1983, *IAU Symp.* 103, “Planetary Nebulae”, p. 233

- Peimbert M. 1997, in IAU Symp. 180, “Planetary Nebulae”, H. Habing and H. Lamers (eds.), in press
- Pena, M., Torres–Peimbert, S., Peimbert, M., Ruiz, M. T., & Maza, J. 1994, ApJ, 428, L9
- Richardson, W. H. 1972, J. Opt. Soc. Am., 62, 55
- Richer, M. G. 1993, ApJ, 415, 240
- Robinson, G. J., Reay, N. K., & Atherton, P. D. 1982, MNRAS, 199, 649
- Sabbadin, F. 1984, A&AS, 58, 273
- Sanduleak, N., MacConnell, D. J., & Philip, A. G. D. 1978, PASP, 90, 621
- Schwarz, H. E., Corradi, R. L. M., & Melnick, J. 1992, A&AS, 96, 23
- Schwarz, H. E., Corradi, R. L. M., & Stanghellini, L. 1993, in IAU Symp. 155, A. Acker & R. Weinberger (eds.), (Dordrecht: Kluwer), p. 214
- Stanghellini, L., Corradi, R. L. M., & Schwarz, H. E. 1993, A&A, 279, 521
- Stanghellini, L. 1995, in “Asymmetric Planetary Nebulae”, Annales of the Israel Physical Society, Vol. 11, eds. A. Harpaz & N. Soker, p. 17
- Vassiliadis, E. 1996, ApJ, 465, 748
- Vassiliadis, E., Dopita, M. A., Morgan, D. H., & Bell, J. F., 1992, ApJS, 83, 87
- Weinberger, R. 1989, A&AS, 78, 301

Figure Captions

Figure 1. Contour plots of the LMC N 192 (a, b) and N 97 (c, d) pre- and post-COSTAR images.

Figure 2. Various point spread functions (PSFs).

Figure 3. Deconvolution of the pre-COSTAR image of N 192 by using each of the PSFs in Fig. 2.

Figure 4. Results of matching and not matching the theoretical PSF to the central star, in N 66.

Figure 5. Narrow-band [O III] FOC images of Magellanic Cloud planetary nebulae.

Figure 6. Parameter distribution of nebular size in pc. (top), nebular expansion velocity in km s^{-1} (middle), and dynamical expansion time in yr (bottom panel) for round (solid), elliptical (dashed) and bipolar/quadrupolar (shaded histogram) MCPNe.

Figure 7. Maximum nebular dimension versus dynamical expansion age for MCPNe which are round (open circles), elliptical (solid circles), and bipolar/quadrupolar (squares).

Figure 8. Nebular electron density versus physical dimension for PNe. Symbols are as in Figure 7. Diameters of optically thick PNe, and of PNe with unknown thickness, can actually be larger than observed, and indicated with arrows.

Figure 9. [O III] surface brightness versus dynamical expansion time. Symbols are as in Figure 7.

Figure 10. Nebular N/O abundance ratio versus dynamical expansion time. Symbols are as in Figure 7. The solid line represents the dividing line between Type I (top quadrant) and non-Type I PNe (bottom quadrant), as described in the text.

Table 1. FOC F/96 Observations of MCPNe in [O III]

Name	RA ^a (J2000)	Dec ^a (J2000)	Filter	Date (UT)	t _{exp} [s]	counts [s ⁻¹]	peak counts [s ⁻¹]	log F [erg cm ⁻² s ⁻¹]
SMC								
N 2	00:32:38.8	-71:41:59	F501N	1991 Jul 09.62	995.9	407.27	0.442	-11.70
N 4	00:34:22.0	-73:13:21	F501N	1993 Apr 28.92	496.8	137.05	0.156	-12.19
N 5	00:41:21.8	-72:45:19	F501N	1991 Jul 09.76	995.9	334.65	0.413	-11.79
N 18	00:46:59.6	-72:49:39	F501N	1992 Nov 25.31	996.9	154.07	0.168	-12.14
L 305	00:56:30.9	-72:27:01	F501N	1993 Apr 26.92	1996.8	87.75	0.360	-12.42
N 67	00:58:37.3	-71:35:49	F501N	1993 Jan 09.85	1996.9	83.33	0.064	-12.40
L 343	00:58:42.6	-72:57:00	F501N	1993 Jul 10.26	1995.8	122.98	0.126	-12.22
L 536	01:24:11.8	-74:02:34	F501N	1993 Jul 06.66	995.8	42.82	0.130	-12.68
LMC								
N 97	05:04:51.9	-68:39:10	F501N	1992 Nov 18.12	1803.2	389.99	0.282	-11.72
			F501N	1994 Feb 02.81	1995.9			-11.77
			F501N ^b	1994 Feb 02.84	995.9			-11.73
N 24	05:06:09.3	-67:45:29	F501N	1992 Dec 12.94	996.9	328.53	0.449	-11.79
N 192	05:09:37.3	-70:49:09	F501N	1993 Mar 03.01	996.8	358.85	0.145	-11.74
			F501N	1994 Feb 06.81	1995.9			-11.77
			F501N ^b	1994 Feb 06.84	995.9			-11.74
WS 12	05:10:50.0	-65:29:31	F501N	1993 Apr 28.86	1996.8	392.38	0.118	-11.72
LM 1-27	05:19:20.7	-66:58:07	F501N	1993 Jun 20.95	1996.8	187.76	0.049	-12.02
N 52	05:28:41.2	-67:33:39	F501N	1992 Nov 18.91	996.9	318.94	0.220	-11.79
N 66	05:36:20.8	-67:18:08	F501N	1991 Jun 26.94	540.3	365.20	0.130	-11.74
			F501N	1993 Jul 10.19	1995.8	325.94	0.247	-11.81
			F501N	1994 Feb 05.30	1995.6			-11.80
			F501N ^b	1994 Feb 06.33	995.9			-11.76
LM 1-61	06:10:25.5	-67:56:21	F501N	1992 Nov 18.84	1778.3	281.64	0.100	-11.85

^aCoordinates: STScI Guide Star Selection System

^bthese filters are really F501N+F1ND

Table 2. Morphology, Diameters, and Optical Depths

Name	SMP	camera	Morph. ^a	θ [arcsec]	D [pc]	opt. depth
SMC						
N 1	1	PC1	R	.241	.068	thin
N 2 ^b	2	FOC	E(Es)	.637	.180	thin
N 4	3	FOC,PC1	B(Bbc)	2.64	.747	thin
N 5	5	FOC	R	.621	.176	thick
N 6 ^b	6	PC1	R	.304	.086	thin
N 18	10	FOC	B(Bbc)	2.64	.747	...
L 305 ^b	21	FOC	E(Es)	3.00	.846	thin
N 67 ^b	22	FOC	B(Bbc)	2.74	.774	thick
L 343	23	FOC	B(Bbc)	2.61	.738	...
L 536 ^b	28	FOC,PC1	E	3.50	.990	thin
LMC						
...	2	PC1	R	.408	.100	thick
N 78	8	PC1	R	thin
LM 2–5 ^b	20	PC1	B(Bbc)	.823	.202	thick
N 97 ^b	21	FOC	Q	1.15	.281	thick
N 24	23	FOC	R	d	d	thin
N 192 ^c	32	FOC	R	1.083	.266	thick
WS 12	35	FOC,PC1	E(inc)	1.59	.391	thick
WS 16	40	PC1	E(Es)	.783	.192	thick
LM 1–27	45	FOC	E(inc)	2.36	.578	thick
N 122 ^b	47	PC1	E?	.412	.101	thin
N 52	66	FOC	E(Es)	1.08	.266	...
...	72	PC1	B	...		thin
N 60	76	PC1	R	thin
N 69	85	PC1	R	thin
N 215 ^b	87	PC1	B(Bbc)	1.01	.248	thick
... ^b	96	PC1	B(Bbc)	.905	.222	thick
LM 1–61	97	FOC	R(Rs)	1.18	.289	thin

Table 2—Continued

Name	SMP	camera	Morph. ^a	θ [arcsec]	D [pc]	opt. depth
------	-----	--------	---------------------	----------------------	-----------	------------

^aR=Round, E=Elliptical, B=Bipolar, Q=Quadrupolar, Rs=Round with (inner) structures, Es=Elliptical with (inner) structures, Einc=Elliptical incomplete, Bbc=Bipolar core

^bType I PN

^cpre- and post-COSTAR FOC images

^dsee text, § 3.2.

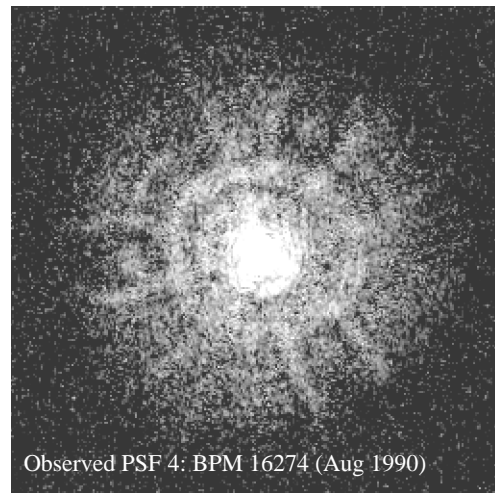
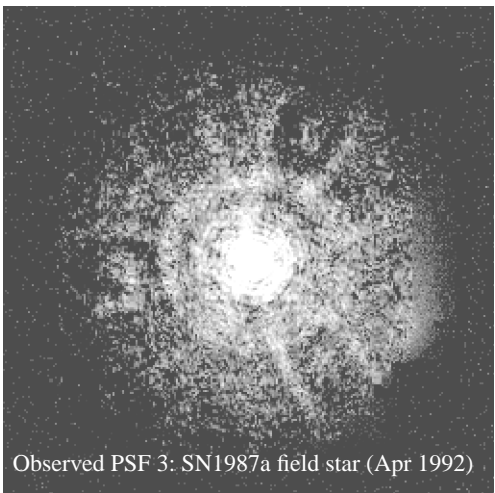
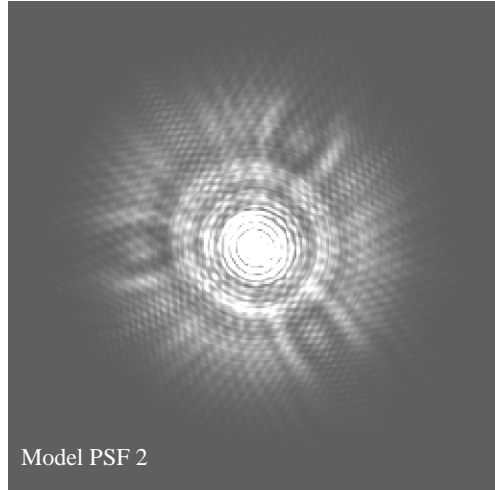
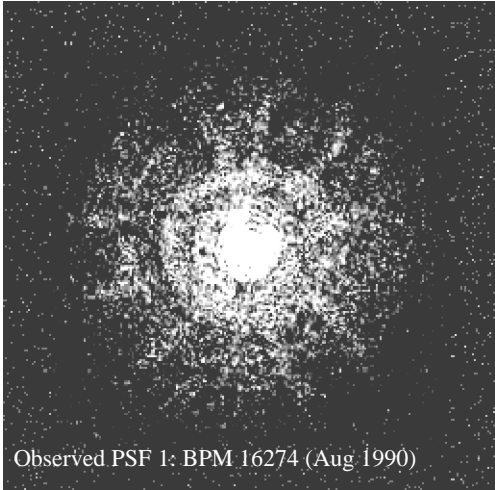
Table 3. Ellipticities, Expansion Velocities, and Dynamical Times

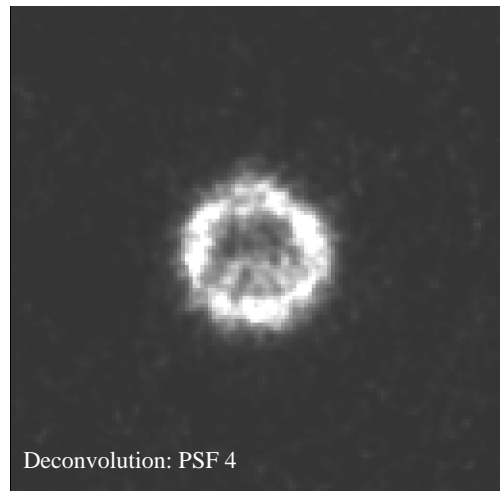
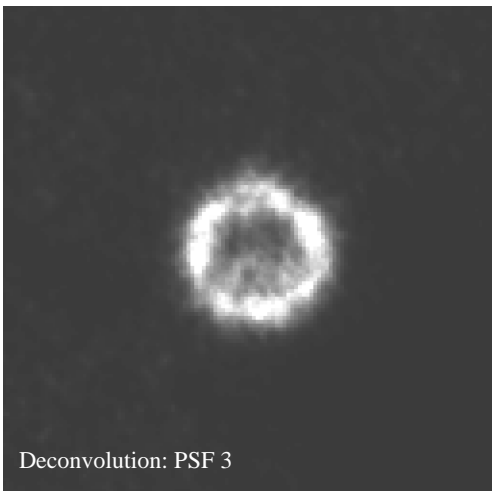
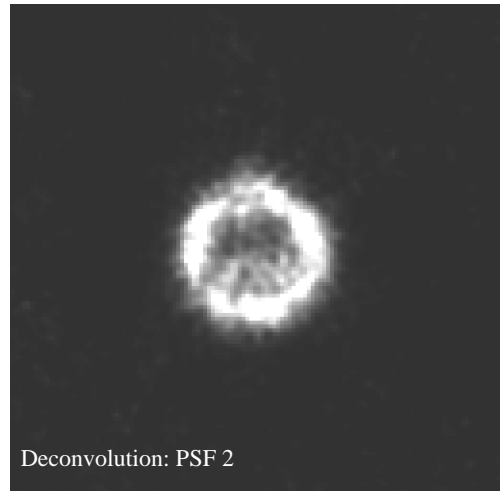
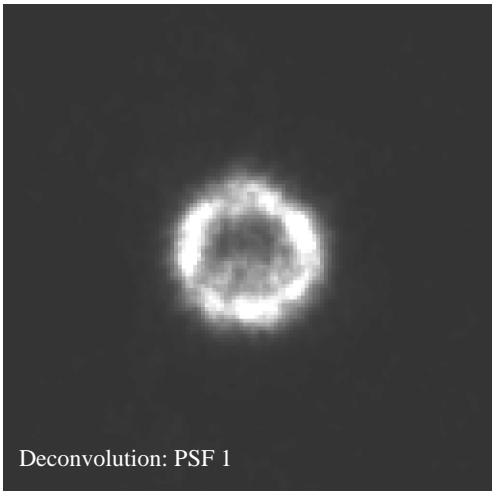
Name	q	V_{exp} [km s ⁻¹]	$\tau_{\text{dyn,yr}}$ [10 ³ yr]
SMC			
N 1	1.0	8.46	3.94
N 2	.92	17.7	4.98
N 4	.69	18.1	20.2
N 5	1.0	16.0	5.38
N 6	1.0	19.3 ^a	2.18
N 18	.80	13.2	27.7
L 305	.90	19.3	21.4
N 67	.71	27.9	13.6
L 343	.94	17.4	20.8
L 536	.80	29.3	16.5
LMC			
SMP 2	1.0	5.44	9.01
N 78	1.0	13.9	...
LM 2–5	1.0	14.2	6.98
N 97	1.0	27.0	5.11
N 24	1.0	11.5	...
N 192	1.0	23.2	5.60
WS 12	.82	22.7	8.44
WS 16	.64	30.0	3.14
LM 1–27	.75	20.2	14.0
N 122	.50	43.2	1.14
N 52	.85	12.7	10.3
SMP 72	.64
N 60	1.0	15.9	...
N 69	1.0	6.21	...
N 215	.57	20.6	5.91
SMP 96	.34	33.5	3.25
LM 1–61	1.0	25.3	5.60

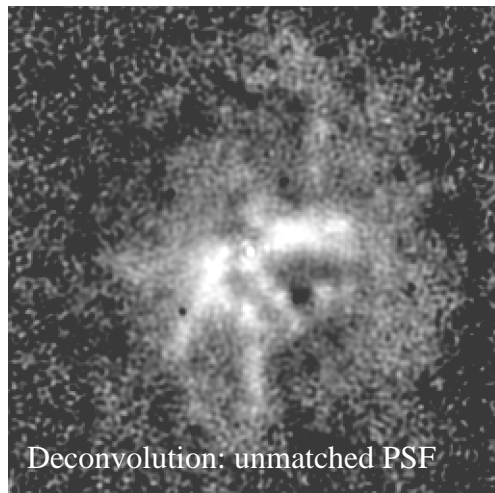
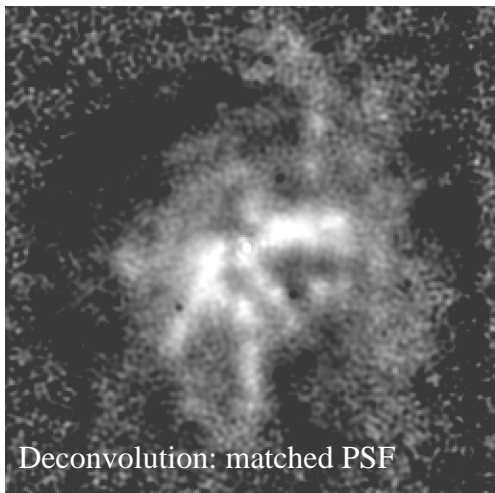
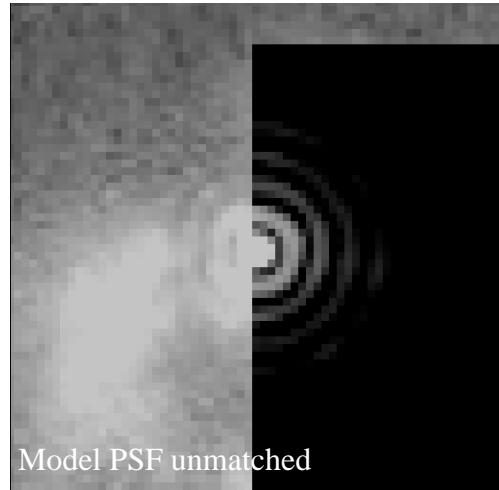
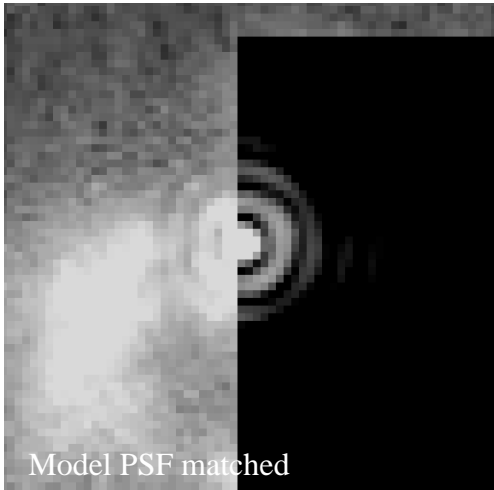
Table 3—Continued

Name	q	V_{exp} [km s ⁻¹]	$\tau_{\text{dyn,yr}}$ [10 ³ yr]
------	---	---	--

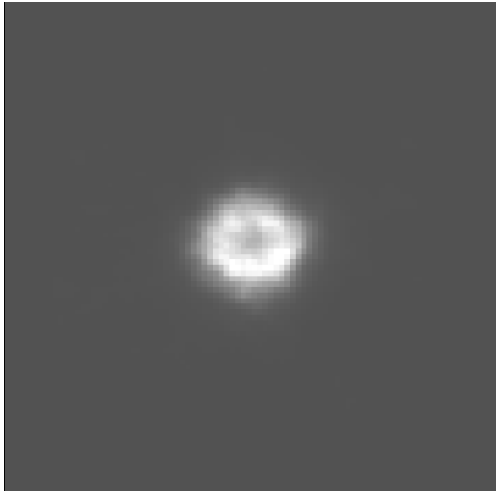
^atwo components: 12.1 and 26.74 km s⁻¹



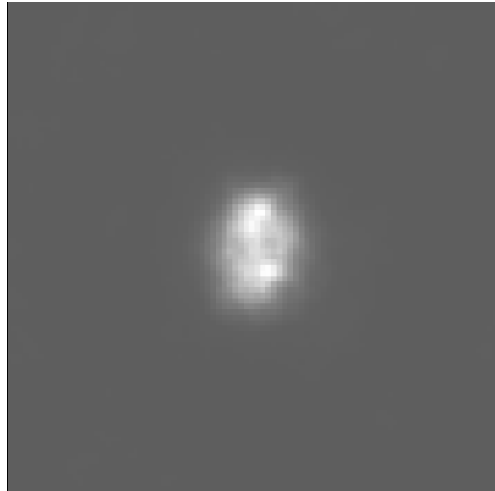




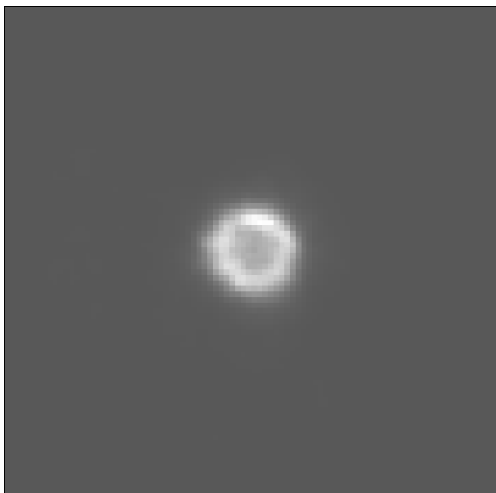
(a) SMC N2



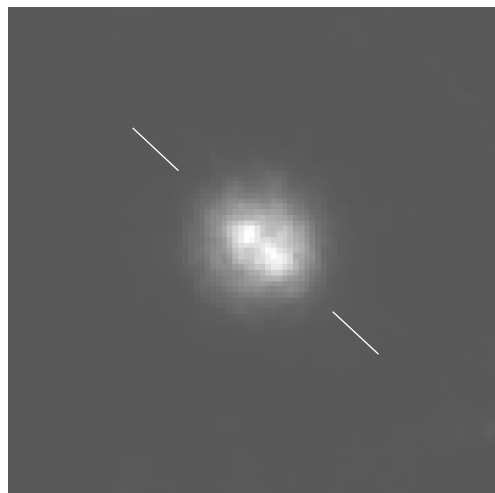
(b) SMC N4



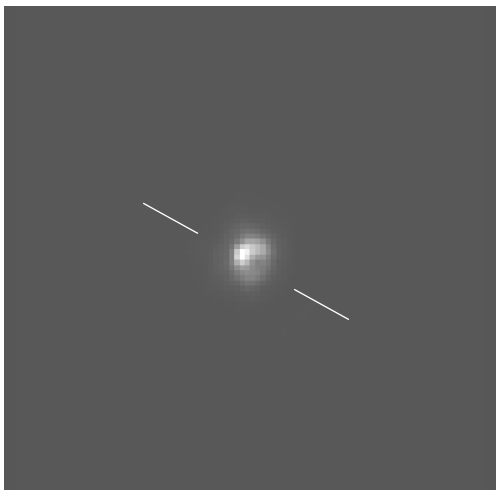
(c) SMC N5



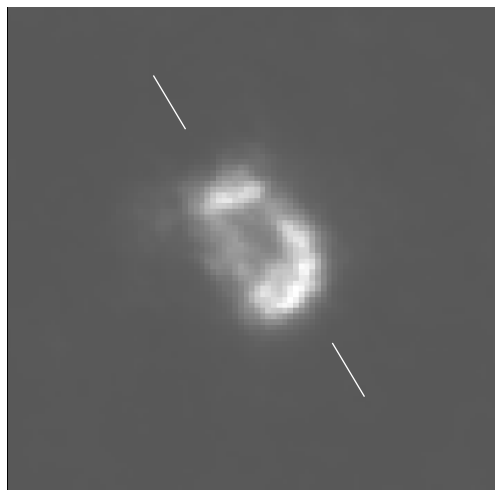
(d) SMC N18



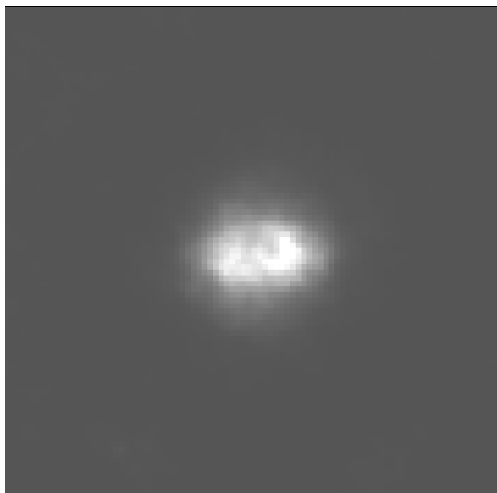
(e) SMC L305



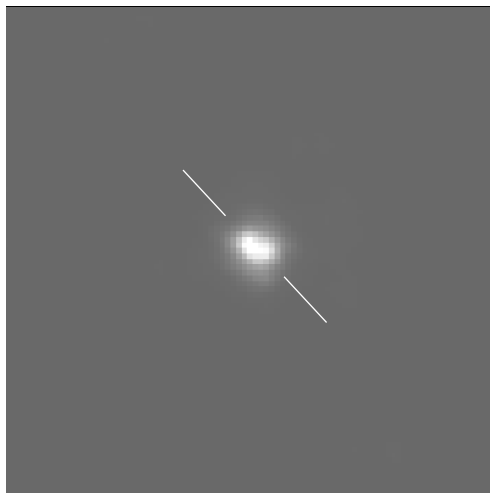
(f) SMC N67



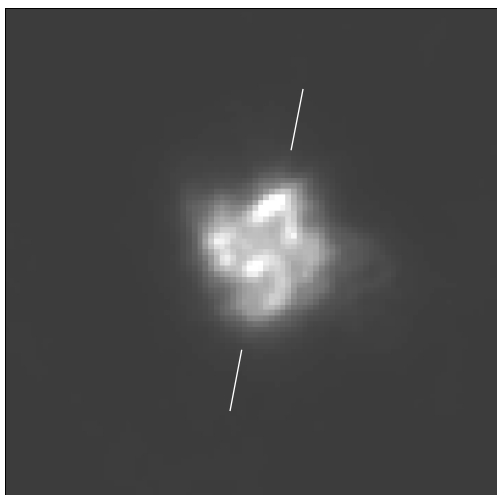
(g) SMC L343



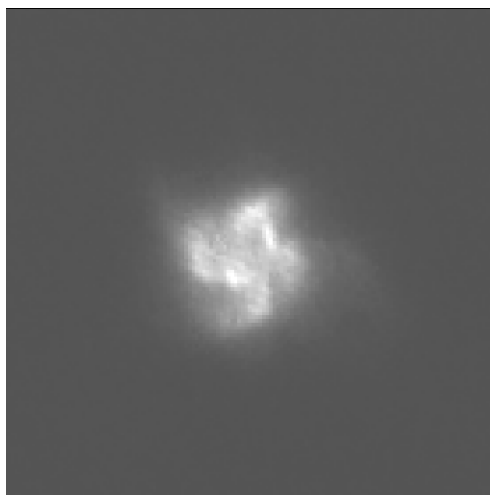
(h) SMC L536



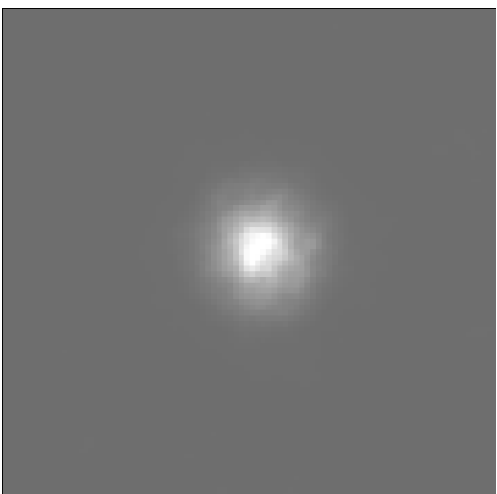
(i) LMC N97



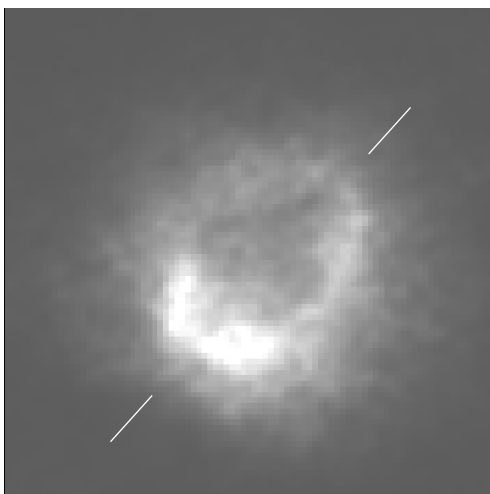
(j) LMC N97, Post-COSTAR



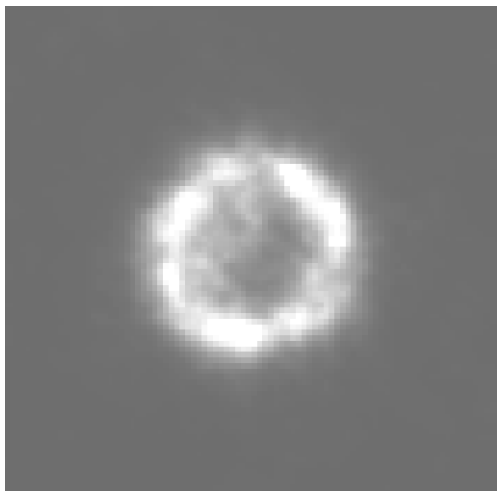
(k) LMC N24



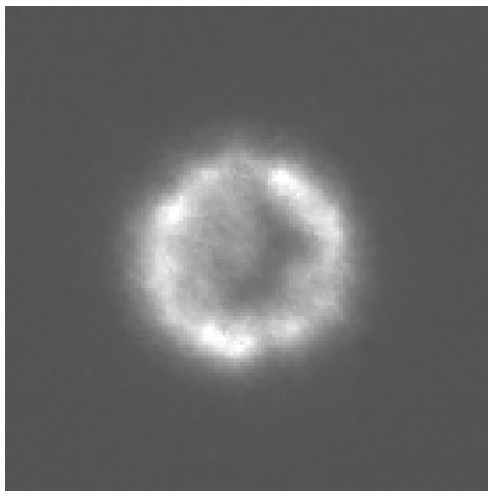
(l) LMC WS12



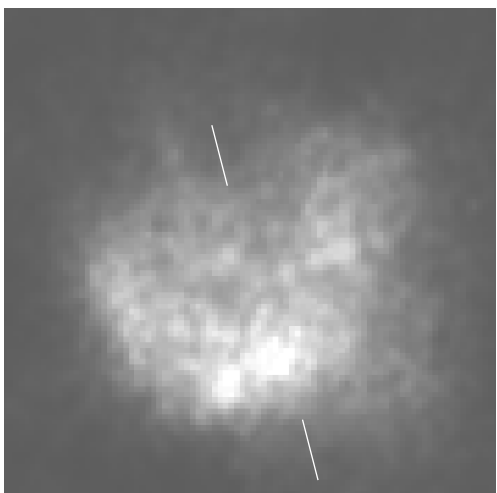
(m) LMC N192



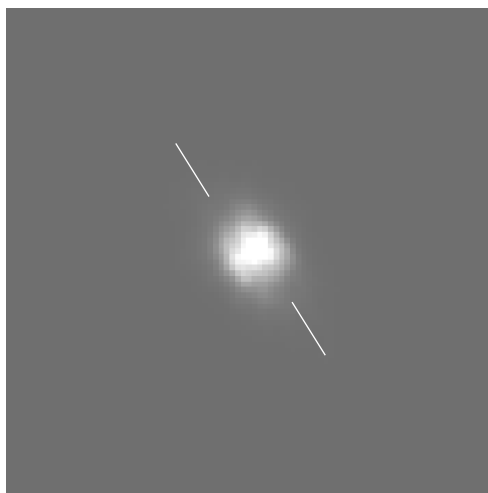
(n) LMC N192, Post-COSTAR



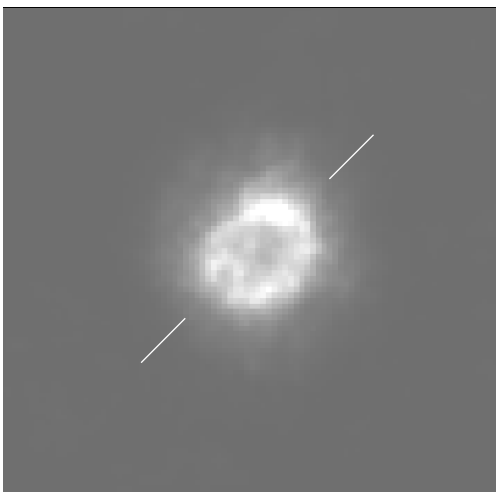
(o) LMC LM1-27



(p) LMC N201 (H β)



(q) LMC N52



(r) LMC LM1-61

